Hugoniot, sound velocity, and shock temperature of MgO to 2300 GPa

C. A. McCoy, M. C. Marshall, D. N. Polsin, D. E. Fratanduono, P. M. Celliers, D. D. Meyerhofer, and T. R. Boehly

Phys. Rev. B **100**, 014106 — Published 24 July 2019

DOI: 10.1103/PhysRevB.100.014106

Hugoniot, sound velocity, and shock temperature of MgO to 2300 GPa

C. A. McCoy[1,2,3*], M. C. Gregor[4], D. N. Polsin[2], D. E. Fratanduono[4], P. M. Celliers[4],

D. D. Meyerhofer[5] and T. R. Boehly[2]

[1]*Sandia National Laboratories, Albuquerque, NM 87185-1195, USA*

[2]*Laboratory for Laser Energetics, University of Rochester,*

Rochester, NY 14623-1299, USA

[3]*Department of Mechanical Engineering, University of Rochester,*

Rochester, NY 14627, USA

[4]*Lawrence Livermore National Laboratory, Livermore, CA 94550, USA*

[5]*Los Alamos National Laboratory, Los Alamos, NM 87545, USA*

MgO is a major constituent of the MgO-FeO-SiO2 system that comprises the Earth's mantle and that of super-Earth exoplanets. Knowledge of its high-pressure behavior is important for modeling the more complex compounds. This paper presents measurements of the principal Hugoniot, sound velocity, and temperature of MgO, shocked to pressures of 710 to 2300 GPa using laser-driven compression. The Hugoniot and temperature measurements compare favorably to previous results constraining the shock response of MgO at extreme conditions. The Grüneisen parameter was calculated from the Hugoniot and sound velocity data and found to be underpredicted by tabular models. The sound velocity of liquid MgO is overpredicted by models implying that the quantity of partial melt required to match decreased wave speeds in ultra-low velocity zones in the lower mantle may be less than previously assumed and experiments at lower-mantle pressures are needed.

I. Introduction

High-pressure equation-of-state (EOS) measurements are fundamental to understanding material properties at conditions relevant to planetary science[1-5], hypervelocity impact[6, 7], and inertial confinement fusion.[8] In particular, high-pressure experiments can be used to describe the material properties of mantle and core constituents for terrestrial planets.[1-3, 9-13] These experiments provide insights that can be used in developing models of planetary interiors, which are then used to explain seismic data[10-15] and geophysical properties such as magnetic field generation[3], plume generation,[14, 15] mantle convection[11], and ultra-low velocity zones (ULVZs).[12, 15]

Advances in facilities, diagnostics, and EOS standards have increased the precision and range of conditions accessible in dynamic compression experiments. Steady planar shock and controlled ramp compression, coupled to modern interferometric techniques, have been demonstrated using both lasers[1, 8, 16-19] and pulsed power[4, 20, 21] as drive sources, decreasing the experimental uncertainty at extreme pressures relative to earlier explosive-driven[22, 23] techniques. The EOS of quartz has been constrained both on and off the Hugoniot, enabling its use as a high-precision standard for shock experiments.[21, 24, 25] This has enabled the development of analysis techniques that can extract more information than available in earlier shock and release experiments and provide constraint of derivative quantities as well as discrete points.

A key derivative quantity that describes the off-Hugoniot properties of a material is its sound velocity under compression. When coupled with Hugoniot measurement, the sound velocity can be used to derive the Grüneisen parameter, which then enables calculation of off-Hugoniot states.[26-29] Measurements of the sound velocity behind a shock front allow for calculation of the bulk and shear moduli in solids,[30, 31] the fluid bulk modulus, and identification

of high-pressure phase transitions.[9, 30, 31] Traditional sound velocity measurements relied on the overtake of a rarefaction wave from the back surface of an impactor at the shock front. This technique has been demonstrated using gas gun[9, 31, 32] and pulsed power[28] launched impactors, but is less useful for laser-driven shocks. Recently, Fratanduono *et al*[26, 33] and McCoy *et al*[27] demonstrated a technique to measure the sound velocity through an analysis of perturbations to the shock velocity created by an unsteady ablation pressure. This technique enables the use of laser-driven shocks for high-pressure sound-velocity experiments and allows for cross-platform comparison of results.

An end member of the MgO-FeO-SiO_2 series, MgO is one of the primary constituents of the Earth's mantle and a likely component of super-Earth exoplanet interiors.[1-5, 10-13, 34] At ambient conditions, MgO exists in a crystalline structure, periclase, then undergoes a solid-solid phase transition with increasing pressure prior to melting along the Hugoniot.[2-5] The Hugoniot and sound velocity of solid MgO have been extensively studied in dynamic compression experiments[35-42], however, only the principal Hugoniot and its temperature have been studied above the melt transition. This has been done through impact and impedance match experiments and decaying shocks.[2-5] Those experiments constrained the thermodynamic properties of MgO to the principal Hugoniot but provided no information about off-Hugoniot behavior.

Seismic observations of the core-mantle boundary (CMB) layer indicate the existence of ULVZs[12, 43] where wave velocities are significantly reduced (by up to 30%) relative to the surrounding mantle. Static measurements of the shear velocity in heated diamond anvil cells indicated that the lower mantle is composed primarily of silicate perovskites[11, 13], $(Mg,Fe)SiO_3$, but the decreased velocity in ULVZs can be attributed to multiple causes. Models of ULVZs include: iron-enriched perovskites[44], the presence of elemental metals from the outer core[45],

and/or partial melting[43]. Static measurements by Wicks *et al*[12] indicate that the presence of iron-rich oxides can account for the decreased wave speeds in ULVZs at CMB pressures, however the exact mechanism leading to iron-enrichment is unknown. Conversely, preheated shock measurements of MgO exhibit solid sound velocities greater than predicted by models, with partial melting a likely cause for anomalously low wave velocity observed at ~240 GPa.[41] Knowledge of the sound velocity of liquid oxides and perovskites provides information on quantity of partial melt required to match seismic observations of ULVZs. This would enable construction of a model that can match all observations by combining partial melt with iron-enriched perovskites.

We present measurements of the Hugoniot, sound velocity, Grüneisen parameter, and temperature in MgO shocked to liquid in the pressure range 710 to 2300 GPa. These pressures are relevant to lower-mantle properties in super-Earth exoplanets, such as GH876d[46] and provide benchmarking data for geophysical models. The Hugoniot and sound velocity measurements were referenced to α-quartz using the most recent model from Desjarlais, Knudson, and Cochrane.[25] An updated linear Hugoniot fit was calculated for liquid MgO and agrees well with previous measurements and SESAME EOS[47] and LEOS tables. Conversely, neither the sound velocity nor Grüneisen parameter measurements are adequately reproduced by either model. Furthermore, geophysical models[13] fail to reproduce the sound velocity, underscoring the need for future experiments at Earth-relevant pressures.

II. Experimental method:

Experiments were conducted at the OMEGA EP[48] laser facility at the University of Rochester's Laboratory for Laser Energetics. In long-pulse operation, OMEGA EP is a 4-beam frequency-tripled Nd:glass laser, operating at a wavelength of 351 nm that can deliver up to 5000

J per beam with pulse lengths up to 10 ns. These experiments used a temporally square pulse with 4-5 ns duration to drive a steady shock into the target. The focal spots were smoothed using distributed phase plates[49] with planar diameters of either 750 or 1100 μm, resulting in on-target laser intensities of ~0.6 to 1.4 × 10^{14} W/cm^2.

The targets were planar stacks consisting of an ablator layer, baseplate, and samples as shown in Figure 1(a). These targets used optically flat, *z*-cut, α-quartz baseplates that were 3 mm square and ~60 μm thick. A 20 μm thick layer of parylene-N (CH) was deposited on the front (laser-side) of the baseplate to act as a low-Z ablator with which the drive laser interacts. This both enhances the ablation pressure and decreases the hard x-ray production from the laser drive, compared to the laser hitting the quartz directly. 1-D magnetohydrodynamics simulations with the code LILAC[50] indicate that preheat from x-rays and hot electrons should be limited to <100 K in the MgO, which has a negligible impact on the Hugoniot states reached in these experiments.

Adjacent samples of single-crystal α-quartz (ρ_0 =2.65 g/cm^3, n=1.547) and single-crystal MgO ([100] periclase, Asphera Inc., ρ_0 =3.584 g/cm^3, n=1.742) (each 1.0 mm × 1.5 mm × 0.2 mm thick) were mounted to the back surface of the quartz baseplate. X-ray fluorescence measurement of the MgO samples indicated >99.9% purity, with the remainder being predominately CaO. An ultra-low viscosity, UV-cured epoxy was used to mount the samples to the quartz baseplate, with pressure applied during curing to minimize the thickness (<3 μm) of the glue layer. A MgF_2 antireflective coating was applied to the back of each sample to minimize Fresnel reflections at the surface and maximize the amount of VISAR probe light reflecting off the shock fronts within the samples.

Two instruments were used to diagnose the conditions of the shock in both the quartz and MgO. A line-imaging velocity interferometry system for any reflector (VISAR)[51-54] measured the velocity of the shock front. The OMEGA EP VISAR uses a Nd:YAG probe laser, frequency-doubled to operate at 532 nm, with the return signal propagated through an interferometer and recorded with a streak camera. An example of the VISAR data is shown in Figure 1(b). The line-imaging VISAR measures phase changes, due to Doppler shifts, in the light reflected off the target and represents them as a series of spatially resolved fringes in the streak image. In these experiments, the quartz and MgO are shock-melted into partially metallic fluids; the probe reflects off the shock front and VISAR provides instantaneous tracking of the shock velocity. The fringe intensity provides a measurement of reflectivity relative to the initial intensity determined by Fresnel reflections at interfaces in the target. The return signal is split into two VISARs, each of which has a different velocity sensitivity, measured in velocity-per-fringe (VPF), to resolve 2π ambiguities in phase. In these experiments, the VPFs were 2.671 km/s/fringe and 4.375 km/s/fringe in the quartz and 2.378 km/s/fringe and 3.896 km/s/fringe in the MgO. Uncertainties in velocity measurements were estimated to be ~3% of a fringe. Preheating of the MgO could decrease the index of refraction by up to 1%, which was added in quadrature to the estimated uncertainty. The streak cameras used 9- and 15-ns sweeps resulting in temporal resolutions of ~30 and ~50 ps, respectively.

The optical emission from the shock front was measured with a streaked optical pyrometer (SOP)[55, 56] which collects both self-emission from the shock front and luminescence in the unshocked material over the wavelength range 590 to 850 nm. The data are shown in Figure 1(c). The SOP data were combined with the VISAR data to provide the optical emission as a function of shock velocity. Using the reflectivity of the shock front, as measured with VISAR,

the emissivity was used in a gray-body approximation to determine the shock temperature from the SOP data. At the time of these experiments, the OMEGA EP SOP was not absolutely calibrated and a relative calibration similar to done by Falk *et al*[57] was determined using the emissivity of the quartz shock front, which has been previously measured[58, 59] with the absolutely calibrated OMEGA SOP.[55, 56] The error in temperature measurement is estimated to be 10-15% from the uncertainties in relative calibration, MgO reflectivity, and the recorded intensity on the streak camera.

III. Analysis:

III. a) Hugoniot

Hugoniot states in MgO were measured using the impedance-matching (IM) technique[8] The pressure, P, and particle velocity, u_p, are determined at the interface between a standard material with a known EOS and the material of interest (in this case MgO), with those quantities assumed to be continuous across that interface. By measuring the shock velocity, U_S, in both the standard and sample and knowing the initial conditions (denoted by subscript 0), the density, ρ, and energy, E, behind the shock are calculated from the Rankine-Hugoniot relations:[60]

$$\rho = \frac{\rho_0 U_S}{U_S - u_p}, \tag{1}$$

$$P = \rho_0 U_S u_p, \text{ and} \tag{2}$$

$$E = E_0 + \frac{1}{2}\left(P + P_0\right)\left(\frac{1}{\rho_0} - \frac{1}{\rho}\right). \tag{3}$$

In these experiments, the initial state of the α-quartz standard was determined from the shock speed (U_S) measured by VISAR in the quartz baseplate before the shock reached the MgO. The quartz $U_S - u_p$ relationship from Desjarlais, Knudson, and Cochrane[25] was used.

Since MgO has greater impedance than quartz, the shock transmitted into the MgO generated a reflected shock in the quartz to maintain continuity across the interface. This reshocked the quartz to higher pressure, with the equilibrium $\left(P, u_p\right)$ state determined from the intersection of the quartz reshock Hugoniot and the MgO Rayleigh line (Eq. 2).

A Mie-Grüneisen EOS of the form

$$P = P_H + \Gamma\rho\left(E - E_H\right) \tag{4}$$

where Γ is the Grüneisen parameter and P_H and E_H are the pressure and energy at density ρ along the 'reference' Hugoniot was used to model the quartz reshock. The effective Grüneisen parameter and linear $U_S - u_p$ fit from Ref. 25 were used to model the quartz reshock. While these fit parameters were developed to model the quartz release, the pressure difference between the quartz and MgO is small and the systematic uncertainty in the calculation should be within the random error calculated with the Monte Carlo technique.

The behavior across the glue layer was modeled using the zeroth-order correction[33]

$$U_{S,f}^{M} = \frac{\left\langle U_S^M \right\rangle}{\left\langle U_S^Q \right\rangle}\delta U_S^Q + U_{S,i}^{M} \tag{5}$$

where $U_{S,i}^{M}$ and $U_{S,f}^{M}$ are the shock velocity in the MgO before and after correcting for the glue layer, respectively. The value of $U_{S,i}^{M}$ was taken 100-300 ps after shock breakout into the MgO to account for ring-up across the glue bond. δU_S^Q is the change in quartz shock velocity across the glue, and $\left\langle U_S^M \right\rangle$ and $\left\langle U_S^Q \right\rangle$ are the average shock velocity in the MgO and quartz samples. The zeroth-order correction has been demonstrated to have a lower uncertainty and be less sensitive to perturbations[61] than the linear extrapolation technique.[8]

III. b) Sound Speed

The MgO sound velocity was measured using the perturbed wave technique referenced to a quartz standard.[27, 33] In this technique, a temporally varying shock is driven into the target and perturbations to the shock velocities in the MgO sample and quartz standard are related to infer sound speed in the shocked materials. The perturbations are propagated through the target as acoustic waves and interactions with shock fronts or material interface treated as Doppler effects. This produces a dilation or compression in the arrival times of successive perturbations as they propagate through a target; these dilations and compression are used to determine the sound velocity.

Because quartz has lower impedance than MgO and is reshocked when the shock transits the interface, acoustic perturbations propagate through the reflected shock prior to arriving at the leading shock front. This compresses the temporal spacing of the perturbations because the acoustic waves are propagating in the opposite direction of the reflected shock. The compression is described in terms of the Mach number, $M = \frac{u_f}{c_s}$, where u_f is the velocity of the reflected shock in the mass-coordinate frame and $c_s^2 = \left(\frac{dP}{d\rho}\right)_s$ is the isentropic sound velocity. Relative to the compressed fluid behind the shock front, the Mach number can be written as

$$M = \frac{\Delta P}{\Delta u_p \rho c_s} \tag{6}$$

where ΔP and Δu_p represent the change in pressure and particle velocity across the shock front. The spacing of perturbations at the shock front Δt_S can then be determined from Doppler shifts to be

$$\Delta t_S = \frac{1}{1 \pm M} \Delta t_0 \,, \tag{7}$$

where Δt_0 is the perturbation spacing after transmission through the previous interaction in a target (initial spacing for first interaction) and the sign denotes the direction of shock propagation: towards (+) or away from (-) the source. For the reflected shock, the perturbations then propagate through the material behind the shock (downstream) to an interface and are dilated by a factor of $\Delta t_i = \left(1 + M_d\right) \Delta t_S$.

The perturbations in these experiments were driven by reverberations in the CH ablator. Because CH has significantly lower impedance than quartz, the initial shock reflects off the quartz baseplate back towards the ablation surface where the pressure releases to the ablation pressure launching a rarefaction wave into the target. The acoustic wave reverberates between the quartz baseplate and the ablation front for the duration of the laser pulse. Each time the wave reaches the CH-quartz interface, the pressure jump when the wave is reflected transmits a weak perturbation into the quartz. This reflected compression wave then reaches the ablation front and releases with a subsequent rarefaction being launched into the target. When the compression waves overtake the shock front, they impart a small increase to the shock pressure (<5%) which then decays to the ablation pressure upon the subsequent rarefaction overtake. This sequence continues until the laser pulse ends and the ablation pressure goes to zero.

Because the perturbation profile was driven by reverberations and depends on mass ablation, the absolute spacing could not be precisely calculated. The perturbation spacing at the shock front in the MgO can be related to the adjacent quartz witness using a scale factor, $F = \frac{\Delta t_2}{\Delta t_1}$, where subscripts 1 and 2 represent the quartz and MgO, respectively. The quartz witness provides a measurement of the perturbation profile at the shock front, which is

backwards-propagated to the CH-quartz interface then forwards-propagated to the shock front in the MgO. Combining the dilation factors for both sides of the target determines the Mach number for the shocked MgO,

$$M_M = 1 - \frac{\left(1 - M_{SQ}\right)\left(1 + M_{RQ,d}\right)}{F\left(1 + M_{RQ,u}\right)}\ , \tag{8}$$

where M_{SQ} and M_{RQ} are the Mach numbers for the singly-shocked quartz and reshocked quartz and the subscripts *d* (downstream) and *u* (upstream) denote the fluid with respect to which the Mach number is calculated. 1-D hydrodynamic simulations indicate that because the first acoustic wave transits the glue after ring-up has completed, the wave does not propagate through any rarefaction or re-shock. Hence, the glue can be treated as two material interfaces, which have a transmission coefficient of 1 and do not factor into Eq. 8.

The *F* factor was determined using the profile-matching technique described in Ref. 27. By definition, the profile-matching region began when the shock transited the quartz baseplate-MgO interface and terminated when the reflected shock from the quartz-MgO interface overtook the shock front. The region of interest (ROI) for the quartz sample had an unconstrained termination point since no reflected shock existed on that side of the target. These experiments had approximately constant shock pressures and the velocity perturbations (ΔU_S), were determined by subtracting off the average shock velocity. This differs from the technique used in Ref. 27, where a linear trend was used to account for an overall temporal variation in the shock velocity. Velocity deviation profiles were smoothed using a weak smoothing spline to reduce random noise in the extracted signal and the *F* factors were extracted separately for each of the two VISAR legs. The uncertainty in the *F* factor was estimated from the difference in those two values which gave a value of ~2.2%. For the two shots where profile-matching didn't

converge for both VISARs, the uncertainty of the converged profile was assumed to be double that.

III. c) Uncertainty quantification

A Markov-chain Monte Carlo (MCMC) method was used to propagate the uncertainty in observed parameters through the Hugoniot and sound speed analysis. The independent variables in the simulations were the measured shock velocities in the quartz and MgO, the quartz Hugoniot and release models, and the *F* factor from profile-matching. The uncertainty propagation calculated the uncertainty in pressure, particle velocity, and density from the quartz models (uncertainty in the quartz sound speed was calculated from the pressure and density uncertainties) and measured velocities then fed those values into the sound speed analysis. The final values and uncertainties for both the Hugoniot and sound speed were determined from 10^5 independent calculations of the results.

IV. Results and Discussion:

IV. a) Hugoniot

The MgO Hugoniot was measured with thirteen experiments ranging in pressure from 710 to 2300 GPa, given in Table I and shown in Figures 2(a and b). At the lowest pressures, these results (yellow diamonds) overlap conditions previously reported by Root *et al*[4] (blue circles) and Miyanishi *et al*[5] (black squares). At higher pressure, these results extend the measured MgO Hugoniot to pressures twice that reached in previous experiments. These data are in good agreement with the previous work for pressures up to 1180 GPa, the maximum pressure achieved in the earlier results from Root *et al*[4] that were generated by the direct impact of magnetically-accelerated flyers on the Sandia *Z* machine[62] with calibrated copper and aluminum standards into MgO samples. The agreement between the present results and those of

Root provides a cross-platform consistency check between direct impact and laser-driven IM techniques.

A new $U_S - u_p$ relationship for liquid MgO (Table II) was calculated using a weighted least-squares linear fit to the present data and Root *et al*[4] for pressures above 620 GPa, the optimized breakpoint between coexistence and liquid phase in their work. The data from Miyanishi *et al*[5] and McWilliams *et al*[2] (open squares) were not included due to uncertainties more than twice as large as those from either Root or this work. These uncertainties resulted in the Miyanishi and McWilliams data being unable to distinguish between different models or fits. The present fit (solid yellow line) is in good agreement with the Root data for the entire range where the data exists. At pressures unconstrained by Root *et al*[4], the previous liquid fit (long-dashed blue line) is too stiff for the present results; this is particularly true for the three values for pressures greater than 1800 GPa, which do not agree with the Root fit at their level of uncertainty. The earlier fit to gas gun data (dotted red line) used by McWilliams *et al*[2] is clearly stiffer than both the present results and those of Root *et al*[4] for MgO shocked above the melt transition.

The results and experimental fit were compared to the SESAME 7460[47] (dashed green line) and LEOS 2190, a QEOS-based[63] model with extensions[64], (dashed-dotted purple line) equation of state tables for MgO. Both tables exhibit approximately identical behavior along the principal Hugoniot in the $U_S - u_p$ plane. However, in the $P - \rho$ plane, which is more sensitive to variations in density along the Hugoniot, the SESAME 7460 table is ~0.5% stiffer than LEOS 2190 at a given pressure. The experimental results are in good agreement with both tables over the entire range of pressures where data exists. When restricting the comparison to only the highest-pressure results, SESAME exhibits a slightly softer behavior than the data, but still falls

within the 1σ uncertainty of the three highest pressure results. The LEOS table lies within 1σ of two of the three highest pressure measurements and is within 0.5% of the density of the highest-pressure result. This agreement is surprising when considering that no data for the liquid phase existed at the time at which the tables were constructed. Previous results have demonstrated that without experimental results to constrain EOS tables above the shock-melting transition, the models could be off by as much as 10%.[21, 27, 65]

In the $U_S - u_p$ plane, both the SESAME 7460 and LEOS 2190 tables fall within the 1σ uncertainty of the present fit (approximately the width of the line). When looking at the $P - \rho$ plane, the present fit is slightly stiffer than SESAME for pressures below 1200 GPa, then progressively softer at increasing pressures. Compared to LEOS 2190, the experimental fit is stiffer than the tabular model, however both curves converge at ~2400 GPa. The maximum difference between the LEOS model and experimental fit occurs just above the melt pressure and is ~1.5% in density. When compared to the previous experimental fit from Root *et al*[4], the present fit is slightly softer for pressures below 1200 GPa, with an increasing difference at higher pressures. For future experiments, either the present fit or that of Root would be recommended for pressures below 1200 GPa, whereas the present fit is more supported at higher pressures. At pressures greater than 2300 GPa, the LEOS 2190 table would is recommended due to expected curvature in the $U_S - u_p$ relationship at high pressure.[21, 61]

IV. b) Sound Speed

The profile-matching technique was used to determine the isentropic sound velocity behind the MgO shock front for the experiments given in Table I. These measurements constrain the bulk modulus and acoustic properties of liquid MgO at extreme pressure. The reverberating ablator in these experiments generated five perturbations to the velocity of the quartz and MgO

shock fronts shown in Figure 1(b). Using the estimated uncertainty in the *F* factor as determined in Sec. III.c and uncertainties in the Hugoniot state for both quartz and MgO, the MCMC error analysis generated uncertainties of 2-4% in the MgO sound velocity. These uncertainties allowed for the experimental results to discriminate between existing models for MgO. A linear $C_S - u_p$ fit was determined for these data and is given in Table III. Caution should be exercised using the fit at lower pressures than constrained experimentally due to the transition from a pure liquid phase to solid or mixed phases.

Figure 3 shows the experimentally determined liquid MgO sound velocity (yellow diamonds) compared to the SESAME 7460 (dashed green line) and LEOS 2190 (dashed-dotted purple line) EOS tables, as well as first-principles molecular dynamics (FPMD) calculations for solid (long-dashed red line) and liquid (long-dashed-dotted red line) by de Koker and Stixrude[34]. The FPMD calculations for the change in sound velocity upon melting (solid red line) are calculated using the Hill average to the Voight and Reuss bounds.[66] All three models overpredict the sound velocity in liquid MgO over the entire pressure range covered by the data. The trend in the LEOS and SESAME tables agrees with the data, with the rate of increase in $C_S(P)$ approximately matching the experiments. The tabular values differ by ~5% from the measurements, corresponding to a deviation of ~1.5σ from the centroid of the data. At high pressure, the experimental data is in agreement with the SESAME and LEOS tables. This implies that the reference value for the liquid sound velocity, which was previously unconstrained by experimental data, in the models is systematically high as $P(\rho)$ and its derivative and $T'(\rho)$ appear to be modeled correctly.

Over the range of the data, the liquid fit (long-dashed-dotted red line) by de Koker and Stixrude[34] significantly overpredicts the sound velocity of molten MgO. Using this fit to

represent the properties of MgO in the mantle implies that the amount of partial melt required to decrease the seismic wave velocity in ULVZs is less than previously assumed, thereby increasing the plausibility of partial melt contributing to ULVZ formation. However, the FPMD liquid fit exhibits a greater rate of change in $C_S(P)$ than either the tabular EOS models or the experimental results. At the CMB pressure of ~130 GPa, extrapolation of the de Koker and Stixrude liquid fit predicts that the sound velocity of liquid MgO is less than that predicted by the SESAME and LEOS tables, however liquid calculations were not made for pressures that low. This difference could result in agreement between the de Koker and Stixrude model and experimental results, increasing the amount of molten material required to corroborate seismic measurements. Measurement of the sound velocity in liquid MgO at CMB conditions would require shock compression preheated to temperatures above 2300K, the highest temperature achieved to date,[41, 42] or laser-heated static compression, both of which are outside the scope of this study. Such measurement would better enable calculation of the amount of partial melt required to decrease seismic wave velocities to match measurements of ULVZs.

IV. c) Grüneisen Parameter

The Grüneisen parameter of liquid MgO, Γ, was calculated from the Hugoniot state and sound velocity determined in the preceding sections using:

$$\frac{\Gamma}{2V} = \frac{\left(\frac{dP}{dV}\right)_H + \frac{C_S^2}{V^2}}{P_H + \left(\frac{dP}{dV}\right)_H (V_0 - V)}, \tag{9}$$

where $V = \frac{1}{\rho}$ is the specific volume and $\left(\frac{dP}{dV}\right)_H$ is the derivative of pressure with respect to volume along the MgO Hugoniot.[32] These calculations used the updated linear $U_S - u_p$

Hugoniot in Table II with the $P-V$ Hugoniot determined from Eqs. 1 and 2. Values for C_S, P_H, and V were taken from the experimental results and the derivative $\left(\frac{dP}{dV}\right)_H$ was calculated from the linear Hugoniot fit at the observed V. Γ was found to decrease from ~0.9 to ~0.7 over the density range 7.5 to 10 g/cm^3 and plotted with the SESAME 7460 (dashed green line) and LEOS 2190 (dashed-dotted purple line) tables in Figure 4. A best-fit Grüneisen parameter determined from the U_S-u_p and C_S-u_p fits is also shown (solid yellow line).

The decreasing trend exhibited in Figure 4 agrees with the general assumption that Γ decreases with increasing density. When comparing to the SESAME and LEOS tables, it is evident that both tables underpredict the experimental results. As the SESAME table exhibits a larger value of Γ than LEOS, it is closer to the data and is within the uncertainty of ~25% of the results. However, the best fit to the data is 1.5-2σ above the prediction from the SESAME table. The discrepancy between the tables and the experimental results is driven primarily by the density difference along the Hugoniot, with the underprediction of the sound velocity below 1300 GPa a contributing factor. At densities lower than those covered by these experiments, both tables and a fit to these data are likely invalid because they will not represent the mixed-phase or solid regions that are present for densities below 7.2 g/cm^3.[4] For increasing density, the Grüneisen parameter and sound velocity measurements approach the SESAME and LEOS table.

IV. d) Temperature

The temperature of shocked MgO was measured for all shots using the SOP diagnostic and the grey body approximation for the reflectivity. A velocity-averaged temperature was computed from the time-resolved VISAR and SOP data for each shot. The velocity binning was 1/10 the peak-to-valley velocity difference in the reverberating state. A single-binned average

temperature and shock velocity is given in Table IV. The average velocity spans the entire streak record of the MgO and includes shock decay at later time, resulting in lower average velocities than the Hugoniot values given in Table I and large uncertainties representing the 1σ spread in sampled velocity and temperature. The averaged temperatures (solid yellow lines) are given in Figure 6 and compared to previous experimental work by Bolis *et al*[3] (dotted red line) and McWilliams *et al*[2] (long-dashed brown line), as well as density functional theory (DFT) calculations from Root *et al*[4] (blue circles) and the SESAME 7460 (dashed green line) and LEOS 2190 (dashed-dotted purple line) EOS tables.

For all but the two highest-pressure shots, these results agree well with the previous decaying shock experiments and DFT calculations. On the highest pressure shots, the measured emission corresponds to temperatures ~10^4 K greater than the previous work; this could imply that the MgO sample was preheated by the drive laser and hence was no longer along the principal Hugoniot. However, a preheated sample would exhibit slightly different compressive characteristics, which would be evident in either the Hugoniot or sound velocity. From Figures 2 and 3, these two points do not show any deviation from the next-highest pressure measurement, which implies that preheat is not the cause of this higher temperature. Another possible source of the increased response is UV-Vis fluorescence, however, studies indicated that over the duration of the experiment, the contribution would be negligible.[67] The other potential cause for a higher temperature measurement is the use of the adjacent quartz witness for the temperature calibration. The temperature at these shock velocities in the quartz witness exceeded those constrained by Hicks *et al*[58] (reanalyzed by Celliers *et al*[59]), such that extrapolation of the fit was required. This extrapolation could misrepresent the quartz temperature used in the relative calibration of the SOP diagnostic, which would affect these MgO results. Revisiting these

results with higher-pressure quartz calibration or absolute calibration could verify the accuracy of the highest-pressure MgO temperature measurements.

IV. e) Specific heat

By measuring the Hugoniot, Grüneisen parameter, and shock temperature, the specific heat at constant volume, C_V, of liquid MgO can be directly calculated. As described by Keeler and Royce[68], the specific heat is given as

$$C_V = \frac{\left(\frac{dE}{dV}\right)_H + P}{\left(\frac{dT}{dV}\right)_H + \Gamma\frac{T}{V}}. \tag{10}$$

Because the temperature measurement represented a velocity-averaged state rather than the impedance match state, P and V were determined from the best-fit linear Hugoniot for the average shock velocity. Similarly, $\left(\frac{dE}{dV}\right)_H$ and $\left(\frac{dT}{dV}\right)_H$ were evaluated at the calculated V from the Hugoniot fit and a temperature fit to these data as well as that of McWilliams *et al*[2] and Bolis *et al*.[3] The velocity-averaged C_V is normalized as $\frac{C_V}{Nk_B}$ where N is the number of atoms per unit mass and k_B is the Boltzmann constant. These results are included in Table IV and shown in Figure 6.

These calculations of the specific heat (yellow diamonds) indicate that the specific heat is approximately constant at $\frac{C_V}{Nk_B} \approx 4.55$ for temperatures between 15,000-65,000 K. However, the SESAME 7460 (dashed green line) and LEOS 2190 (dashed-dotted purple line) tables both indicate that C_V increases with temperature over the entire region. The experimental uncertainty is too large to reject the increasing behavior in SESAME and LEOS over this range of

temperatures. McWilliams[2] (long-dashed brown line) found that C_V decreases from 13,000-25,000 K then increases before reaching a local maximum at ~45,000 K; this behavior was attributed to changes in atomic packing, similar to that identified in silica.[58] The approximately constant behavior in the present results is likely the result of measuring discrete temperature points and fitting the temperature as a function of specific volume. This introduced a smooth trend in the derivative $\left(\frac{dT}{dV}\right)_H$, rather than one where the curvature changes as seen in the original McWilliams data[2]. If this behavior is physical, it indicates that the change in atomic packing occurs smoothly over the entire temperature range rather than in discrete temperature bands. The peak at ~28,000 K in the SESAME table corresponds to the anomalous behavior in the Grüneisen parameter shown in Figure 4 and is potentially an electronic or structural change that isn't observed in the experimental data or LEOS table.

The specific heat is dominated by the derivatives of $E(V)$ and $T(V)$, both of which contribute 2-5 times the corresponding terms (P and $\Gamma\frac{T}{V}$, respectively). Hence, the uncertainty will be proportionately affected by the uncertainty in the derivatives. A Monte Carlo method similar to that described in Section III.c was used to account for correlation between uncertainties and determine the total uncertainty (random + systematic) in C_V to be ~9-13%.

V. Conclusions:

The Hugoniot and sound velocity of shock-compressed MgO were measured for pressures from 710 to 2300 GPa. The Hugoniot and sound velocity were determined by impedance matching to α-quartz using the most recent release model by Desjarlais, Knudson, and Cochrane[25] and observing the overtake of acoustic perturbations at the shock front in both the MgO and quartz windows. Temperature measurements were made by normalizing the MgO

shock emission to that of the shocks in the quartz witness using the Celliers[59] reanalysis of Hicks *et al*.[58] The Hugoniot was found to agree with previous results and SESAME and LEOS equation-of-state tables for MgO, while extending the constrained pressures by a factor of 2. An updated $U_S - u_p$ relationship was derived for liquid MgO and was found to be slightly stiffer than the SESAME 7460 and LEOS 2190 tables at high pressure. The temperature measurements are in good agreement with previous shock-temperature measurements, whereas the tabular models overpredict the temperature for a given pressure. Calculated values of the specific heat imply that the specific heat remains approximately constant with increasing temperature between 15,000-65,000 K, whereas the SESAME and LEOS tables exhibit a steady increase with respect to temperature. At the highest experimental pressures, the Hugoniot, sound velocity, and temperature data are in agreement with the SESAME and LEOS tables.

The experimental sound velocity is ~5% less than predicted by both EOS tables and decreases at a faster rate with decreasing pressure than that in the models. The Grüneisen parameter exhibits better agreement with SESAME 7460 than LEOS 2190. Sound speed calculations by de Koker and Stixrude[34] significantly overpredict the sound velocity along the Hugoniot over the entire range of the data. These results can be used to benchmark material models that are used to understand the interior of the Earth and super-Earth exoplanets. This implies that in the lower mantle, the quantity of partial melt required to decrease the sound velocity to ULVZ levels may be less than previously estimated, and measurement of the sound velocity of liquid MgO and its melting point at lower-mantle pressures is needed.

VI. Acknowledgements

We thank the OMEGA target fabrication and experimental operations groups for their efforts towards these experiments. Sandia National Laboratories is a multimission laboratory

managed and operated by National Technology & Engineering Solutions of Sandia, LLC, a wholly owned subsidiary of Honeywell International Inc., for the U.S. Department of Energy's National Nuclear Security Administration under contract DE-NA0003525. This material is based upon work supported by the Department of Energy National Nuclear Security Administration under Award Number DE-NA0001944, the University of Rochester, and the New York State Energy Research and Development Authority.

VII. References

1. F. Coppari, R. F. Smith, J. H. Eggert, J. Wang, J. R. Rygg, A. Lazicki, J. A. Hawreliak, G. W. Collins and T. S. Duffy, Nature Geoscience **6** (11), 926-929 (2013).

2. R. S. McWilliams, D. K. Spaulding, J. H. Eggert, P. M. Celliers, D. G. Hicks, R. F. Smith, G. W. Collins and R. Jeanloz, Science **338** (6112), 1330-1333 (2012).

3. R. M. Bolis, G. Morard, T. Vinci, A. Ravasio, E. Bambrink, M. Guarguaglini, M. Koenig, R. Musella, F. Remus, J. Bouchet, N. Ozaki, K. Miyanishi, T. Sekine, Y. Sakawa, T. Sano, R. Kodama, F. Guyot and A. Benuzzi□Mounaix, Geophys. Res. Lett. **43** (18), 9475-9483 (2016).

4. S. Root, L. Shulenburger, R. W. Lemke, D. H. Dolan, T. R. Mattsson and M. P. Desjarlais, Phys. Rev. Lett. **115** (19), 198501 (2015).

5. K. Miyanishi, Y. Tange, N. Ozaki, T. Kimura, T. Sano, Y. Sakawa, T. Tsuchiya and R. Kodama, Phys. Rev. E **92** (2), 023103 (2015).

6. L. C. Chhabildas, L. N. Kmetyk, W. D. Reinhart and C. A. Hall, Int. J. Imp. Engin. **17** (1–3), 183-194 (1995).

7. E. A. Taylor, J. P. Glanville, R. A. Clegg and R. G. Turner, Int. J. Imp. Engin. **29** (1), 691-702 (2003).

8. M. A. Barrios, D. G. Hicks, T. R. Boehly, D. E. Fratanduono, J. H. Eggert, P. M. Celliers, G. W. Collins and D. D. Meyerhofer, Phys. Plasmas **17** (5), 056307 (2010).

9. J. H. Nguyen and N. C. Holmes, Nature **427** (6972), 339-342 (2004).

10. M. Murakami, Y. Ohishi, N. Hirao and K. Hirose, Earth Planet Sci. Lett. **277** (1–2), 123-129 (2009).

11. M. Murakami, Y. Ohishi, N. Hirao and K. Hirose, Nature **485** (7396), 90-94 (2012).

12. J. K. Wicks, J. M. Jackson and W. Sturhahn, Geophys. Res. Lett. **37** (15) (2010).

13. L. Stixrude, R. J. Hemley, Y. Fei and H. K. Mao, Science **257** (5073), 1099-1101 (1992).

14. T. Komabayashi, K. Hirose, E. Sugimura, N. Sata, Y. Ohishi and L. S. Dubrovinsky, Earth Planet Sci. Lett. **265** (3), 515-524 (2008).

15. K. Burke, B. Steinberger, T. H. Torsvik and M. A. Smethurst, Earth Planet Sci. Lett. **265** (1), 49-60 (2008).

16. R. Smith, J. Eggert, R. Jeanloz, T. Duffy, D. Braun, J. Patterson, R. Rudd, J. Biener, A. Lazicki and A. Hamza, Nature **511** (7509), 330-333 (2014).

17. D. G. Hicks, T. R. Boehly, P. M. Celliers, D. K. Bradley, J. H. Eggert, R. S. McWilliams, R. Jeanloz and G. W. Collins, Phys. Rev. B **78** (17), 174102 (2008).

18. N. Ozaki, T. Ono, K. Takamatsu, K. Tanaka, M. Nakano, T. Kataoka, M. Yoshida, K. Wakabayashi, M. Nakai and K. Nagai, Phys. Plasmas **12** (12), 124503 (2005).

19. S. Brygoo, E. Henry, P. Loubeyre, J. Eggert, M. Koenig, B. Loupias, A. Benuzzi-Mounaix and M. R. Le Gloahec, Nature Materials **6** (4), 274-277 (2007).

20. C. A. Hall, Phys. Plasmas **7** (5), 2069-2075 (2000).

21. M. D. Knudson and M. P. Desjarlais, Phys. Rev. Lett. **103** (22), 225501 (2009).

22. A. C. Mitchell, W. J. Nellis, J. A. Moriarty, R. A. Heinle, N. C. Holmes, R. E. Tipton and G. W. Repp, J. Appl. Phys. **69** (5), 2981-2986 (1991).

23. R. F. Trunin, Physics-Uspekhi **37** (11), 1123-1145 (1994).

24. M. D. Knudson and M. P. Desjarlais, Phys. Rev. B **88** (18), 184107 (2013).

25. M. P. Desjarlais, M. D. Knudson and K. R. Cochrane, J. Appl. Phys. **122** (3), 035903 (2017).

26. D. E. Fratanduono, P. M. Celliers, D. G. Braun, P. A. Sterne, S. Hamel, A. Shamp, E. Zurek, K. J. Wu, A. E. Lazicki, M. Millot and G. W. Collins, Phys. Rev. B **94** (18), 184107 (2016).

27. C. A. McCoy, M. C. Gregor, D. N. Polsin, D. E. Fratanduono, P. M. Celliers, T. R. Boehly and D. D. Meyerhofer, J. Appl. Phys. **120** (23), 235901 (2016).

28. C. A. McCoy, M. D. Knudson and S. Root, Phys. Rev. B **96** (17), 174109 (2017).

29. R. G. McQueen, S. P. Marsh, J. W. Taylor, J. N. Fritz and W. J. Carter, in *High-Velocity Impact Phenomena*, edited by R. Kinslow (Academic Press, New York, 1970), pp. 293–417.

30. D. Hayes, R. S. Hixson and R. G. McQueen, AIP Conf. Proc. **505** (1), 483-488 (2000).

31. J. H. Nguyen, M. C. Akin, R. Chau, D. E. Fratanduono, W. P. Ambrose, O. V. Fat'yanov, P. D. Asimow and N. C. Holmes, Phys. Rev. B **89** (17), 174109 (2014).

32. R. G. McQueen, 20th American Physical Society Topical Conference on Shock Compression of Condensed Matter, 75-78 (1991).

33. D. E. Fratanduono, D. H. Munro, P. M. Celliers and G. W. Collins, J. Appl. Phys. **116** (3), 033517 (2014).

34. N. De Koker and L. Stixrude, Geophys. J. Int. **178** (1), 162-179 (2009).

35. T. S. Duffy and T. J. Ahrens, AIP Conf. Proc. **309** (1), 1107-1110 (1994).

36. T. S. Duffy and T. J. Ahrens, J. Geophys. Res. Solid Earth **100** (B1), 529-542 (1995).

37. D. E. Fratanduono, J. H. Eggert, M. C. Akin, R. Chau and N. C. Holmes, J. Appl. Phys. **114** (4), 043518 (2013).

38. M. S. Vassiliou and T. J. Ahrens, Geophys. Res. Lett. **8** (7), 729-732 (1981).

39. L. Zhang, Z. Gong and Y. Fei, J. Phys. Chem. Solids **69** (9), 2344-2348 (2008).

40. S. P. Marsh, *LASL Shock Hugoniot Data*. (University of California Press, Berkeley, CA, 1980).

41. O. V. Fat'yanov and P. D. Asimow, J. Phys. Conf. Ser. **500** (6), 062003 (2014).

42. O. V. Fat'yanov, P. D. Asimow and T. J. Ahrens, Phys. Rev. B **97** (2), 024106 (2018).

43. T. Lay, E. J. Garnero and Q. Williams, Phys. Earth Planet. Inter. **146** (3), 441-467 (2004).

44. W. L. Mao, Y. Meng, G. Shen, V. B. Prakapenka, A. J. Campbell, D. L. Heinz, J. Shu, R. Caracas, R. E. Cohen, Y. Fei, R. J. Hemley and H.-k. Mao, Proc. Natl. Acad. Sci. U.S.A. **102** (28), 9751-9753 (2005).

45. M. Manga and R. Jeanloz, Geophys. Res. Lett. **23** (22), 3091-3094 (1996).

46. D. Valencia, R. J. O'Connell and D. Sasselov, Icarus **181** (2), 545-554 (2006).

47. S. P. Lyon and J. D. Johnson, Report No. LA-UR-92-3407, 1992.

48. L. J. Waxer, D. N. Maywar, J. H. Kelly, T. J. Kessler, B. E. Kruschwitz, S. J. Loucks, R. L. McCrory, D. D. Meyerhofer, S. F. B. Morse, C. Stoeckl and J. D. Zuegel, Opt. Photonics News **16** (7), 30–36 (2005).

49. Y. Lin, G. N. Lawrence and T. J. Kessler, Opt. Lett. **20** (7), 764-766 (1995).

50. J. Delettrez, R. Epstein, M. C. Richardson, P. A. Jaanimagi and B. L. Henke, Phys. Rev. A **36** (8), 3926–3934 (1987).

51. L. M. Barker and R. E. Hollenbach, J. Appl. Phys. **43** (11), 4669–4675 (1972).

52. L. M. Barker and K. W. Schuler, J. Appl. Phys. **45** (8), 3692–3693 (1974).

53. P. M. Celliers, D. K. Bradley, G. W. Collins, D. G. Hicks, T. R. Boehly and W. J. Armstrong, Rev. Sci. Instrum. **75** (11), 4916–4929 (2004).

54. P. M. Celliers, G. W. Collins, L. B. Da Silva, D. M. Gold and R. Cauble, Appl. Phys. Lett. **73** (10), 1320–1322 (1998).

55. M. C. Gregor, R. Boni, A. Sorce, J. Kendrick, C. A. McCoy, D. N. Polsin, T. R. Boehly, P. M. Celliers, G. W. Collins, D. E. Fratanduono, J. H. Eggert and M. Millot, Rev. Sci. Instrum. **87** (11), 114903 (2016).

56. J. E. Miller, T. R. Boehly, A. Melchior, D. D. Meyerhofer, P. M. Celliers, J. H. Eggert, D. G. Hicks, C. M. Sorce, J. A. Oertel and P. M. Emmel, Rev. Sci. Instrum. **78** (3), 034903 (2007).

57. K. Falk, C. A. McCoy, C. L. Fryer, C. W. Greeff, A. L. Hungerford, D. S. Montgomery, D. W. Schmidt, D. G. Sheppard, J. R. Williams, T. R. Boehly and J. F. Benage, Phys. Rev. E **90** (3), 033107 (2014).

58. D. G. Hicks, T. R. Boehly, J. H. Eggert, J. E. Miller, P. M. Celliers and G. W. Collins, Phys. Rev. Lett. **97** (2), 025502 (2006).

59. P. M. Celliers, P. Loubeyre, J. H. Eggert, S. Brygoo, R. S. McWilliams, D. G. Hicks, T. R. Boehly, R. Jeanloz and G. W. Collins, Phys. Rev. Lett. **104** (18), 184503 (2010).

60. Y. B. Zel'dovich and Y. P. Raizer, *Physics of Shock Waves and High-Temperature Hydrodynamic Phenomena*. (Dover Publications, 2002).

61. C. A. McCoy, M. C. Gregor, D. N. Polsin, D. E. Fratanduono, P. M. Celliers, T. R. Boehly and D. D. Meyerhofer, J. Appl. Phys. **119** (21), 215901 (2016).

62. M. E. Savage, L. F. Bennett, D. E. Bliss, W. T. Clark, R. S. Coats, J. M. Elizondo, K. R. LeChien, H. C. Harjes, J. M. Lehr and J. E. Maenchen, Pulsed Power Conference, 2007 16th IEEE International **2**, 979-984 (2007).

63. R. M. More, K. H. Warren, D. A. Young and G. B. Zimmerman, Phys. Fluids **31** (10), 3059-3078 (1988).

64. D. A. Young and E. M. Corey, J. Appl. Phys. **78** (6), 3748-3755 (1995).

65. M. D. Knudson and M. P. Desjarlais, Phys. Rev. Lett. **118** (3), 035501 (2017).

66. J. P. Watt, G. F. Davies and R. J. O'Connell, Rev. Geophys. **14** (4), 541-563 (1976).

67. Y. Kawaguchi, Solid State Commun. **117**, 17-20 (2001).

68. R. N. Keeler and E. B. Royce, in *Physics of High Energy Density*, edited by P. Caldirola and H. Knoepfel (New York, 1971), pp. 88-93.

Tables:

Table I: Hugoniot and sound velocity measurements for MgO. U_S^Q and U_S^M are the shock velocities for quartz and MgO, respectively; all other quantities listed are for the shocked MgO. Subscripts 1 and 2 denote which VISAR was used to determine the given F value. The uncertainty in F was estimated by averaging the two values for each shot and found to be ~2%. For shots 21302 and 21306, where only one F value was found, the uncertainty was doubled to 4%. *Intermediate data available from authors.

Shot #	U_S^Q (km/s)	U_S^M (km/s)	u_p (km/s)	P (GPa)	ρ (g/cm^3)	F_1	F_2	C_S (km/s)	Γ
21303	19.4±0.2	19.7±0.2	10.0±0.2	711±12	7.30±0.14	1.10	1.12	15.7±0.3	0.93±0.09
21302	22.5±0.2	22.1±0.1	12.3±0.2	976±17	8.08±0.18	1.09	***	16.5±0.5	0.98±0.07
20453	23.1±0.1	22.9±0.1	12.7±0.1	1042±12	8.03±0.12	1.10	1.10	17.2±0.3	0.91±0.06
21307	23.2±0.2	22.9±0.1	12.8±0.2	1049±16	8.10±0.16	1.02	1.06	17.8±0.6	0.85±0.09
20461	24.8±0.1	24.4±0.1	13.9±0.1	1216±11	8.32±0.10	1.09	1.07	18.2±0.4	0.86±0.06
21312	24.8±0.1	24.4±0.1	14.0±0.1	1222±10	8.40±0.11	1.05	1.03	18.5±0.4	0.83±0.06
21309	24.9±0.1	24.4±0.2	14.1±0.1	1231±15	8.46±0.16	1.10	1.06	17.9±0.6	0.90±0.07
21305	26.2±0.2	25.8±0.1	15.0±0.2	1384±20	8.57±0.17	1.01	1.02	19.8±0.5	0.75±0.07
20459	27.1±0.1	26.8±0.1	15.6±0.1	1492±14	8.57±0.12	1.06	1.07	19.9±0.4	0.75±0.06
21310	27.2±0.1	26.6±0.1	15.7±0.1	1498±15	8.80±0.14	1.05	1.04	19.6±0.5	0.81±0.06
21308	29.9±0.1	28.8±0.1	17.7±0.2	1829±20	9.28±0.16	1.04	0.97	21.2±0.7	0.77±0.06
21306	31.6±0.1	30.4±0.1	19.0±0.2	2072±19	9.54±0.15	***	1.00	21.9±0.5	0.76±0.05
21304	33.1±0.1	32.0±0.2	20.1±0.2	2303±26	9.60±0.20	1.01	0.97	23.2±0.6	0.70±0.07

Table II: Fit and covariance matrix parameters for liquid MgO Hugoniot of form $U_S = C_0 + Su_p$ (U_S and u_p in km/s).

C_0 (km/s)	S	$\sigma_{C_0}^2$ (×10^{-2})	σ_S^2 (×10^{-4})	$\sigma_{C_0}\sigma_S$ (×10^{-3})
7.049	1.240	3.047	1.942	-2.414

Table III: Fit and covariance matrix parameters for liquid MgO sound velocity of form $C_S = A + Bu_p$ (C_S and u_p in km/s).

A (km/s)	B	σ_A^2 (×10^{-1})	σ_B^2 (×10^{-3})	$\sigma_A\sigma_B$ (×10^{-2})
7.881	0.752	5.276	2.585	-3.635

Table IV: Velocity-averaged reflectivity, temperature, and specific heat for MgO. $\langle U_S \rangle$ is the average shock velocity over the entire VISAR record in the MgO; its uncertainty is the 1σ bound on instantaneous velocity. $\langle P \rangle$ and $\langle \rho \rangle$ are calculated from $U_S - u_p$ Hugoniot fit given in Table II. $\langle R \rangle$ and $\langle T \rangle$ are the measured shock reflectivity and temperature, respectively, and $\left\langle \frac{C_V}{Nk_B} \right\rangle$ is the normalized specific heat.

Shot #	$\langle U_S \rangle$ (km/s)	$\langle P \rangle$ (GPa)	$\langle \rho \rangle$ (g/cm^3)	$\langle R \rangle$	$\langle T \rangle$ (kK)	$\left\langle \frac{C_V}{Nk_B} \right\rangle$
21303	20.0±0.4	746±39	7.50±0.09	0.036±0.006	18.0±1.8	4.93±0.64
21302	21.6±0.3	909±33	7.85±0.07	0.070±0.009	23.2±2.4	4.74±0.57
21307	22.1±0.3	959±35	7.95±0.07	0.112±0.016	25.0±2.6	4.70±0.55
21312	23.8±0.3	1148±33	8.28±0.05	0.139±0.019	34.4±3.6	4.66±0.50
21309	24.1±0.5	1192±65	8.35±0.10	0.114±0.017	32.0±3.3	4.55±0.48
21305	24.9±0.6	1288±72	8.50±0.11	0.118±0.016	36.1±3.7	4.53±0.46
21310	25.6±0.6	1370±79	8.62±0.11	0.169±0.027	43.1±4.7	4.57±0.48
21308	26.9±0.9	1550±120	8.86±0.16	0.145±0.020	47.5±5.0	4.49±0.41
21306	27.5±0.8	1630±120	8.95±0.14	0.174±0.022	57.2±5.8	4.55±0.41
21304	28.2±1.1	1720±160	9.07±0.18	0.219±0.028	64.0±6.4	4.57±0.43

Figures:

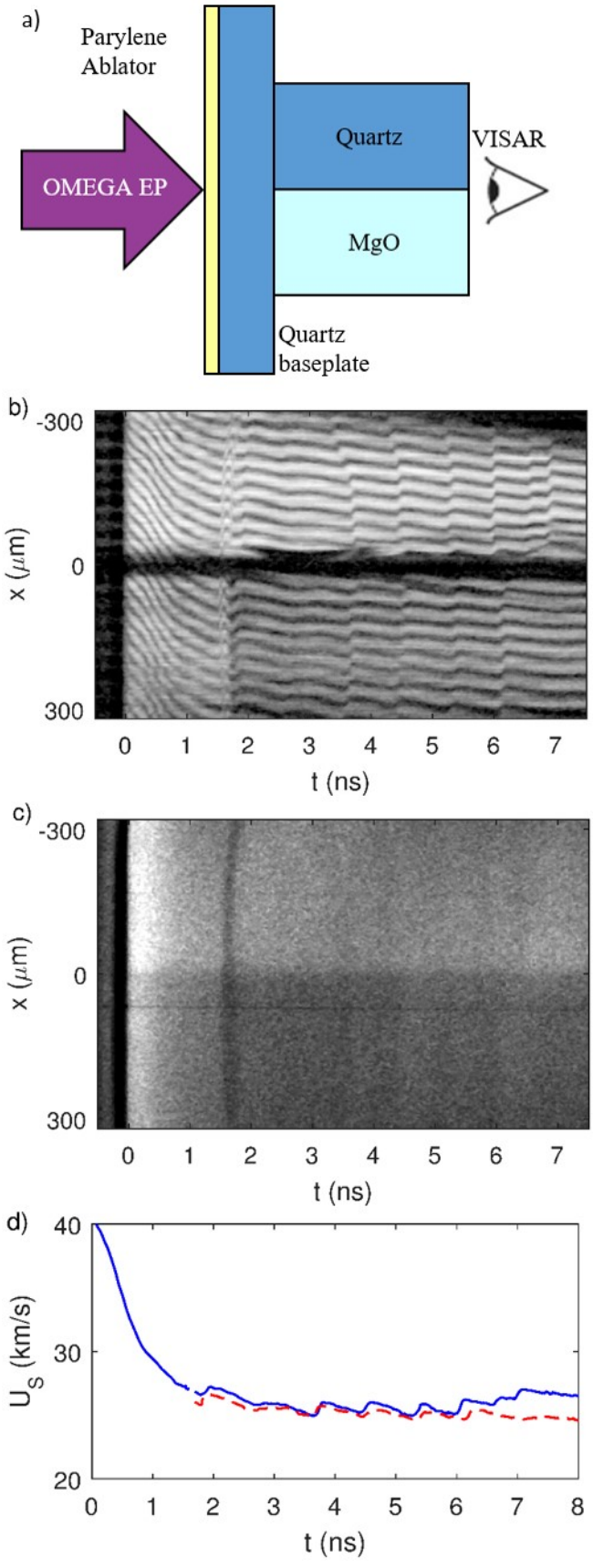
a)
Parylene
Ablator
OMEGA EP
Quartz
MgO
VISAR
Quartz
baseplate
b)
-300
0
300
x (μm)
0 1 2 3 4 5 6 7
t (ns)
c)
-300
0
300
x (μm)
0 1 2 3 4 5 6 7
t (ns)
d)
40
30
20
U_S (km/s)
0 1 2 3 4 5 6 7 8
t (ns)

Figure 1: (a) Target schematic showing parylene ablator, quartz baseplate and quartz and MgO samples. (b) Raw VISAR data for shot 21310; target orientation same as in (a). The VISAR image shows the initial shock decay in the quartz baseplate, with steady-state conditions reached shortly after transiting the baseplate-sample interface. The oscillations from the reverberating ablator are clearly seen across the target, indicating a nominally uniform pressure drive. The difference in fringe intensity in the samples is caused by the difference in reflectivity of the quartz and MgO shock fronts, whereas the difference in the baseplate is related to loss from Fresnel reflections at the quartz-MgO interface. (c) The raw SOP data (orientation same as above) measured the emission from both the quartz and MgO samples for use in a temperature measurement. The pressure oscillations manifest as slight variations in emitted intensity from the shock front in the quartz and MgO. (d) Velocity profiles for quartz (blue solid) and MgO (red dashed) extracted from the raw data in (b). Temporal axes in (b-d) were adjusted to put t_0 at the time where the shock entered the quartz baseplate.

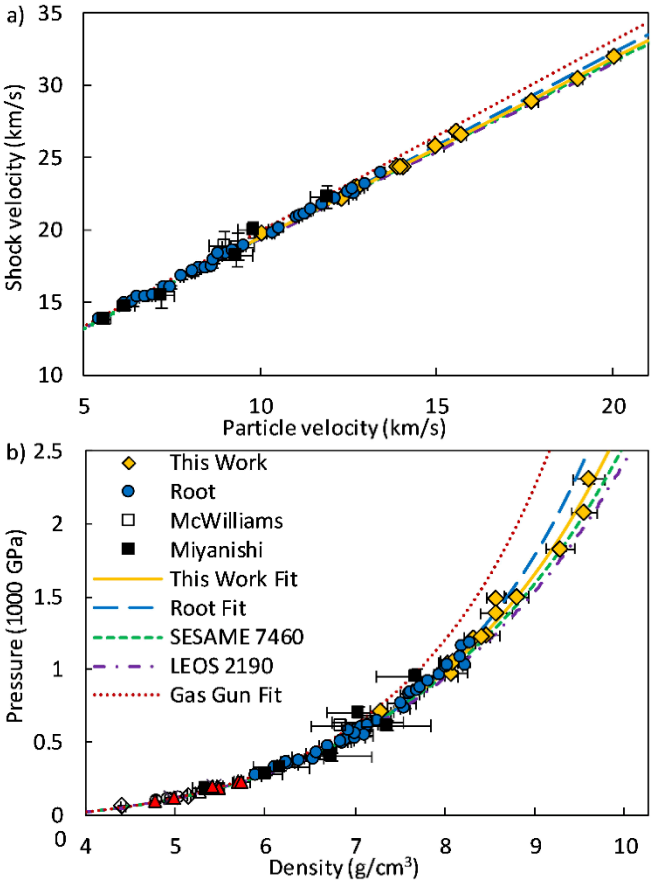

Figure 2: (a) $U_S - u_p$ plot showing Hugoniot measurements for MgO. Experimental results from this work (yellow diamonds) are compared to Root *et al*[4] (blue circles), Miyanishi *et al*[5] (black squares), and McWilliams *et al*[2] (open squares). Linear fits to liquid data from this work (yellow solid) and Root *et al*[4] (blue long-dashed) are shown with tabular results from SESAME 7460[47] (green dashed) and LEOS 2190[63, 64] (purple dashed-dotted) and the extrapolated fit to gas gun data[2] (red dotted). The fit in this work was made using the present results as well as those of Root. (b) The $P - \rho$ Hugoniot indicates that the present work agrees best with SESAME 7460, with LEOS 2190 being slightly soft at high pressure. Compared to experimental fits, Root is too stiff above 1500 GPa, and the gas gun fit does not agree with any high-precision liquid results. Also shown are data for solid MgO from Ref. 35 (open diamonds), Ref. 37 (red triangles), Ref. 38 (open triangles), Ref. 39 ('X'), and Ref. 40 (open circles).

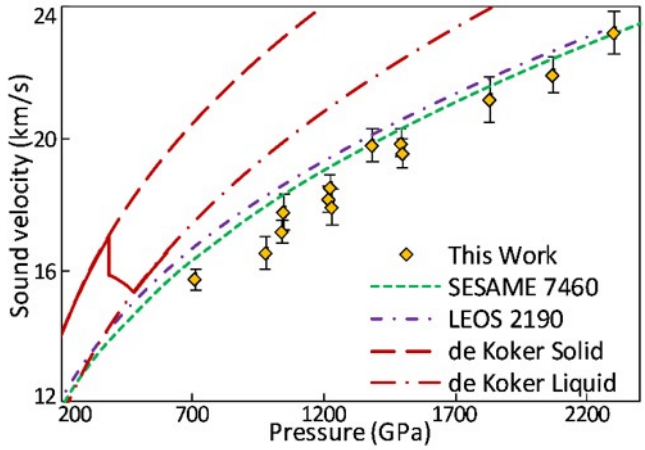

Figure 3: The measured Eulerian sound velocity (yellow diamonds) is systematically lower than tabular models in SESAME 7460 (green dashed) and LEOS 2190 (purple dashed-dotted) for pressures below 1200 GPa along the principal Hugoniot. Extrapolations of molecular dynamics simulations by de Koker and Stixrude[34] significantly overpredict the sound velocity of liquid MgO (red long-dashed-dotted). At lower pressure, where MgO is no longer liquid along the principal Hugoniot, the liquid calculations appear to converge with tabular models. The velocity change upon melting (red solid) is shown using the Hill average of the Voight and Reuss bounds.[66]

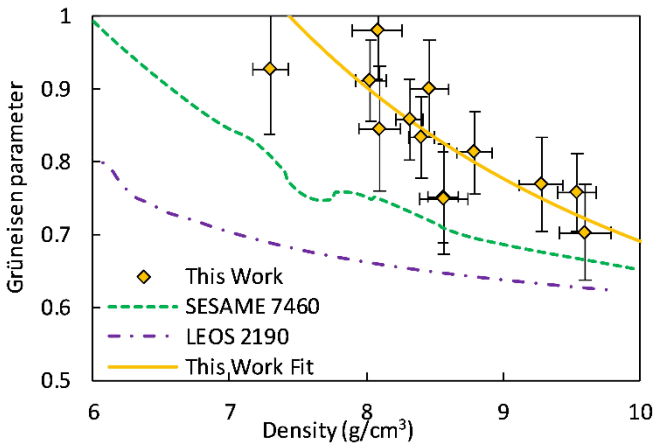

Figure 4: (Lines and symbols same as Figure 3) The Grüneisen parameter in liquid MgO decreases as a function of density, while approaching the theoretical limit of $\Gamma=0.66$. These data better agree with SESAME 7460 than LEOS 2190. The Grüneisen parameter calculated from a best-fit to the principal Hugoniot and sound velocity (solid yellow line) is in excellent agreement with these data and approaches the SESAME and LEOS tables at high compression. Caution should be exercised below the range of the data due to solidification of MgO and both tables being single-phase models.

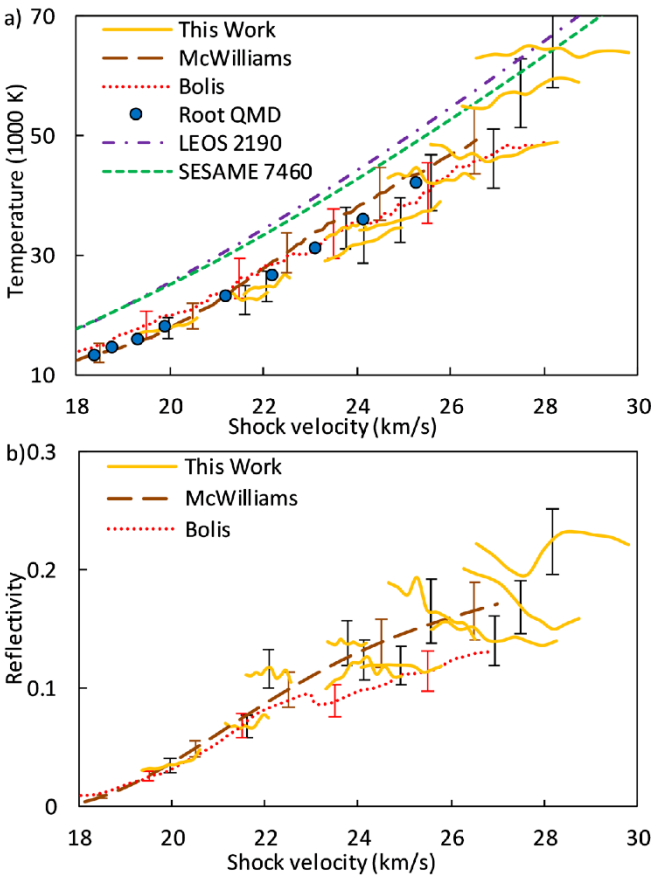

Figure 5: (a) The temperature measurements from this work (yellow lines) are in good agreement with decaying shock measurements by McWilliams *et al*[2] (brown long-dashed) and Bolis *et al*[3] (red dotted) and QMD calculations by Root *et al*[4]. The highest pressure experiments from this work exhibit higher temperatures than the trend mapped by the rest of the data and previous work, which may be related to their temperatures falling outside the range of the relative calibration to quartz[57, 58] for the OMEGA EP SOP diagnostic. Temperature uncertainties from Bolis and McWilliams are shown as red and brown error-bars, respectively. Uncertainty in this work (black error-bars) are maximum values over individual velocity bins. Both SESAME 7460 (green dashed) and LEOS 2190 (purple dashed-dotted) overpredict the shock temperature for a given pressure. (b) The reflectivity measurements from this work agree better with the decaying shock measurements by McWilliams for velocities above 23 km/s and do not support the drop in

reflectivity identified by Bolis. In the highest-pressure experiments, the measured reflectivity fits the same trend exhibited by the rest of the data, implying that an anomaly in reflectivity does not explain the higher temperatures seen in (a).

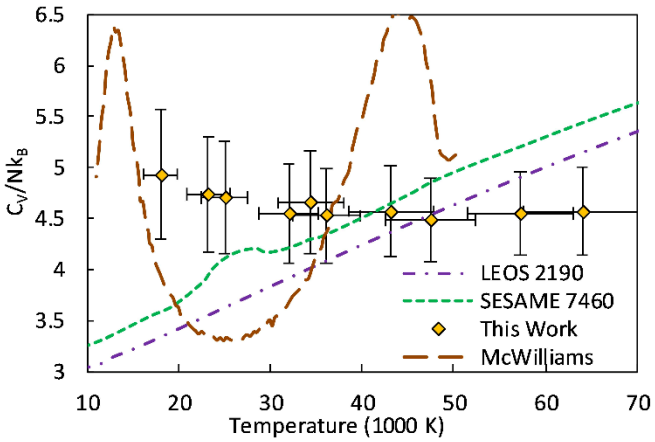

Figure 6: The calculated specific heat from this work (yellow diamonds) is nearly constant for temperatures between 15,000-65,000 K. This differs from the previous calculation of McWilliams (long-dashed brown line) where C_V decreases from 13,000-25,000K then increases prior to reaching a maximum at ~45,000 K. The SESAME 7460 (dashed green line) and LEOS 2190 (dashed-dotted purple line) both find that the specific heat increases with temperature, however SESAME shows anomalous behavior at ~25,000-28,000 K, which corresponds to the abrupt change in the Grüneisen parameter in Fig.4.